

Electrical Tuning of Single Nitrogen-Vacancy Center Optical Transitions Enhanced by Photoinduced Fields

L. C. Bassett,* F. J. Heremans,* C. G. Yale,* B. B. Buckley,* and D. D. Awschalom†

*Center for Spintronics and Quantum Computation,
University of California, Santa Barbara, California 93106, USA*

(Dated: May 29, 2018)

We demonstrate precise control over the zero-phonon optical transition energies of individual nitrogen-vacancy (NV) centers in diamond by applying multi-axis electric fields, via the dc Stark effect. The Stark shifts display surprising asymmetries that we attribute to an enhancement and rectification of the local electric field by photoionized charge traps in the diamond. Using this effect, we tune the excited-state orbitals of strained NV centers to degeneracy and vary the resulting degenerate optical transition frequency by >10 GHz, a scale comparable to the inhomogeneous frequency distribution. This technique will facilitate the integration of NV-center spins within photonic networks.

PACS numbers: 71.55.Cn, 71.70.Ej, 78.56.-a, 81.05.ug

Nitrogen-vacancy (NV) centers in diamond are promising solid-state qubits for emerging quantum technologies, due to their long spin coherence times [1] and fast manipulation rates [2], together with a level structure that allows for straightforward optical initialization and readout of the electronic spin state [3]. Furthermore, in high-quality single-crystal diamond at temperatures below ≈ 25 K [4], sharp zero-phonon-line (ZPL) optical transitions facilitate the coherent coupling between NV-center spins and photons [5, 6]. The integration of NV centers within photonic structures [7] to route single photons and enhance the spin-photon interaction could therefore lead to scalable applications for quantum information processing and secure communication [8].

As solid-state “trapped atoms,” NV centers are sensitive to their local environment. While this sensitivity has enabled nanoscale magnetic [9] and electric [10] metrology, it also exposes individual NV centers to sample inhomogeneities, leading to a distribution of ZPL frequencies within a diamond [11]. The ability to tune these frequencies is crucial for photonic applications, for instance to utilize the selection rules at the C_{3v} symmetry point for spin-photon entanglement [6] or to coherently couple distant NV centers to indistinguishable photons. Through the dc Stark effect, applied electric fields perturb both the ground-state spin [10, 12] and excited-state orbitals [13], providing the means to control the optical transitions.

Here we use micron-scale devices to manipulate electric fields in three dimensions, to compensate the intrinsic local strain and electrostatic fields of individual NV centers and achieve full control of the orbital Hamiltonian. Furthermore, by analyzing the Stark shifts as a function of applied voltages, we infer a surprising amplification and rectification of the local electric field, consistent with electrostatic contributions from photoionized charge traps within the diamond host. By harnessing this reproducible effect, we can tune the NV-center Hamiltonian to arbitrary points across a range comparable to the inhomogeneous ZPL distribution.

The electronic structure of the negatively charged NV center is determined by symmetry, through its point group C_{3v}

[11, 14]. The spin-triplet ground (GS, symmetry 3A_2) and excited states (ES, symmetry 3E) are connected by ZPL transitions around 637.2 nm (1.946 eV). Our experiments are performed at zero magnetic field, where the spin-triplet basis states are $\{|S_x\rangle, |S_y\rangle, |S_z\rangle\}$. A 532 nm (2.3 eV) “repump” beam pulsed at ≈ 300 kHz in a confocal geometry maintains a spin-polarized population in $|S_z\rangle$. Between repump cycles, we count photoluminescence excitation (PLE) photons emitted by the NV center into the redshifted phonon sideband [see Fig. 1(a)] after absorption from a narrow-line red laser tunable across the ZPL transitions. As we scan the red laser frequency, we typically measure two peaks in the PLE spectrum as shown in Fig. 1(b); these correspond to spin-conserving transitions from the GS orbital singlet $|A_2, S_z\rangle$ to the two ES orbital eigenstates $\{|E_1, S_z\rangle, |E_2, S_z\rangle\}$. In a crystal environment with perfect C_{3v} symmetry and zero electric and magnetic fields, these ES orbital states would be degenerate, but the symmetry is generally broken by local crystal strain and by nonuniform electrostatic charge distributions that generate local electric fields.

The dc Stark perturbation to the Hamiltonian, $\hat{H}_{\text{Stark}} = -\hat{\boldsymbol{\mu}} \cdot \mathbf{F}$, describes the interaction between the local electric field \mathbf{F} and the electric dipole operator $\hat{\boldsymbol{\mu}}$. For fixed stress, the strain perturbation can be cast into the same form by isolating components which transform as the irreducible representations of C_{3v} [14]. The combined perturbation has the form $V_{A_1} \hat{O}_{A_1} + V_{E_x} \hat{O}_{E_x} + V_{E_y} \hat{O}_{E_y}$, where \hat{O}_{Γ_a} is an orbital operator transforming as the basis state $|\Gamma_a\rangle$ and

$$\begin{cases} V_{A_1} = S_{A_1} - \mu_{\parallel} F_z \\ V_{E_x} = S_{E_x} - \mu_{\perp} F_x \\ V_{E_y} = S_{E_y} - \mu_{\perp} F_y \end{cases} \quad (1)$$

are the symmetrized field strengths, in terms of fixed strain components S_{Γ_a} , projections of the local electric field F_i , and the reduced matrix elements of the electric dipole operator $\{\mu_{\parallel}, \mu_{\perp}\}$. We choose orbital basis states $\{|E_x\rangle, |E_y\rangle\}$ for the ES which transform like vectors $\{x, y\}$ in the NV-center coordinate system [15], and we ignore the small (≈ 100 MHz) spin-spin coupling between ES spin states $|S_z\rangle$

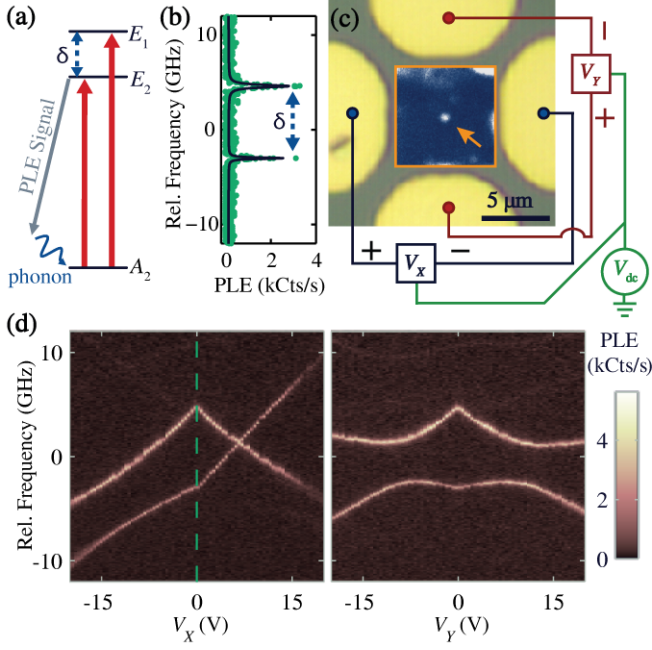


FIG. 1. (a) Simplified energy-level diagram (not to scale) showing only the $|S_z\rangle$ levels of the NV-center ground and excited states, with resonant excitation (red arrows) and redshifted emission (gray arrow) marked. (b) PLE spectrum (points) with no applied bias, marked by dashed line in (d), with a two-Lorentzian fit (solid curve). (c) Micrograph and photoluminescence image (center) of device A, with electrical connections marked. (d) PLE spectra of the 6- μm -deep NV center marked by an arrow in (c) as a function of lateral bias applied symmetrically to the X (left panel) or Y (right panel) gate pairs, with $V_{dc} = 0$ V. In all PLE spectra, the origin of the relative frequency axis is arbitrary.

and $\{|S_x\rangle, |S_y\rangle\}$ [16]. By defining $\hat{H}|A_2, S_z\rangle \equiv 0$, the Hamiltonian in the $\{|E_x, S_z\rangle, |E_y, S_z\rangle\}$ basis can be written as

$$H = (\hbar\omega_0 + \Delta\mu_{\parallel}F_z)\mathbf{I} + \frac{1}{\sqrt{2}} \begin{pmatrix} V_{E_x} & -V_{E_y} \\ -V_{E_y} & -V_{E_x} \end{pmatrix}, \quad (2)$$

where $\hbar\omega_0$ is the natural transition energy including fixed perturbations of A_1 symmetry, and $\Delta\mu_{\parallel} = (\mu_{\parallel}^{\text{GS}} - \mu_{\parallel}^{\text{ES}})$, defined such that both $\Delta\mu_{\parallel}$ and μ_{\perp} are positive. The transition energy eigenvalues take the form $E_{\pm} = h\bar{\nu} \pm \frac{1}{2}h\delta$, where

$$h\bar{\nu} = \hbar\omega_0 + \Delta\mu_{\parallel}F_z, \quad (3a)$$

$$h\delta = \sqrt{2} \left(V_{E_x}^2 + V_{E_y}^2 \right)^{1/2} \quad (3b)$$

are the longitudinal and transverse components due to fields of A_1 and E symmetry, respectively. From Eq. (1), it is clear that a local electric field can cancel the transverse components of intrinsic strain to restore C_{3v} symmetry to the system, and from Eq. (3a) we see that an electric field F_z applied along the NV-center symmetry axis shifts the energy of both transitions by the same amount.

We first investigate these effects using device A, shown in Fig. 1(c), consisting of four Ti-Pt-Au gates fabricated on the

diamond surface. The sample is a 0.5-mm-thick single-crystal diamond grown by chemical vapor deposition with <5 ppb nitrogen content (ElementSix), irradiated with 2 MeV electrons ($1.2 \times 10^{14} \text{ cm}^{-2}$) and then annealed at 800 $^{\circ}\text{C}$ to create NV centers. Measurements are performed in a continuous-flow cryostat operating at ≈ 20 K. Symmetric biases V_X and V_Y applied as shown in Fig. 1(c) produce lateral electric fields F_X and F_Y in the $[110]$ and $[\bar{1}10]$ crystal directions, respectively, while a common dc bias generates fields in the $[001]$ out-of-plane (Z) direction. The sample (x, y, z) and NV-center (x, y, z) coordinate systems are uniquely related for a given NV-center projection from the $\langle 111 \rangle$ family [17].

Figure 1d contains a series of PLE spectra showing the optical resonances of the NV center marked in Fig. 1(c), as a function of separate biases V_X and V_Y with $V_{dc} = 0$ V. The lateral biases are applied as symmetrically pulsed square waves at 1 kHz, with PLE photons binned according to polarity. While the response to static lateral bias is qualitatively similar, this technique separates slow photoinduced charging effects from the dielectric response as discussed below. Two features are evident in the data: first, we observe an unexpected “kink” at zero bias, and second, the resonances cross at $V_X \approx 7$ V, demonstrating that we can indeed restore C_{3v} symmetry to the system. We explore both of these features below with additional experiments.

The kink at zero bias reflects an asymmetry in the local electric field vector as a function of polarity, i.e., $\mathbf{F}(+V) \neq -\mathbf{F}(-V)$. We argue that this asymmetry results from the photoionization of charge traps in the diamond host. Even in high-quality single-crystal synthetic diamonds, deep defects such as vacancy complexes and substitutional nitrogen have important effects on the material’s electronic properties [18]. In particular, substitutional nitrogen atoms form donor levels ≈ 1.7 – 2.2 eV below the conduction band edge [19], and the timescale for charge transport through these levels is very long (hours) even in nitrogen-rich diamond at room temperature [20]. These traps are easily ionized by the 532 nm repump beam ($\approx 100 \mu\text{W}$) which is 4–5 orders of magnitude stronger than the red laser (≈ 1 nW). When voltages are applied, this leads to a long-lived nonequilibrium charge distribution in the illuminated volume of the sample, which can either amplify or screen the local electric field.

As a simplified one-dimensional demonstration, we present in Fig. 2(a) the Stark-shift response of an NV center 13 μm below the surface of a second diamond sample irradiated and annealed under similar conditions, but patterned with a global top gate of the transparent conductor indium-tin-oxide (device B). As the top-gate bias is stepped in a loop over ≈ 160 min, we observe hysteresis in the response characteristic of ≈ 1 h charge-relaxation timescales. Furthermore, by comparing the magnitudes of the Stark shifts due to biases applied laterally across an 8 μm gap [Fig. 1(d)] and vertically across the 0.5 mm sample thickness [Fig. 2(a)], we find that, when the top-gate bias is negative, the local electric field below the top gate appears to be amplified by roughly an order of magnitude over dielectric predictions [17]; conversely, the field appears

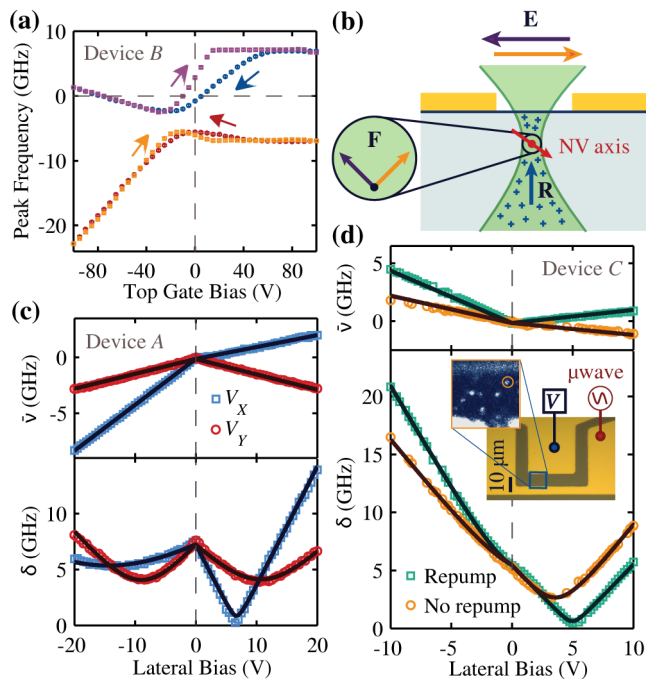


FIG. 2. (a) Stark-shift hysteresis loop for an NV center 13 μm below a transparent top gate, as a function of top-gate voltage. Points mark the transition frequencies from a two-Lorentzian fit to a PLE spectrum at the corresponding voltage and color-coded arrows indicate the sweep direction. (b) Schematic of the local electric fields in a lateral geometry. Photoionized charge traps in the illuminated volume contribute a rectified field \mathbf{R} predominantly in the $+Z$ direction, which adds to the dielectric field \mathbf{E} to shift the direction of the local field \mathbf{F} . (c) dc Stark components $\bar{\nu}$ and δ (points) extracted from fits of the PLE spectra in Fig. 1(d), with a combined fit according to the model described in the text (solid curves). (d) dc Stark components (points) and fits (solid curves) measured both with (green squares) and without (orange circles) the 532 nm repump excitation. Inset: Micrograph and photoluminescence image of device C, with electrical connections marked. The 7- μm -deep NV center measured in (d) is circled. In all cases, marker sizes slightly exceed measurement uncertainties.

to be completely screened above a threshold bias, where the response is flat. The response of an NV center in device A to variations of V_{dc} is qualitatively similar [17], and both are consistent with a picture in which positive charges in the illuminated volume below the NV center rectify the Z component of the electric field.

We can incorporate these charging effects into a phenomenological model capturing the essential features of our observations. As depicted in Fig. 2(b), the local electric field for an NV center between two surface gates is composed of a dielectric component roughly parallel to the sample surface and a rectified component due to photoionized charge that is mainly out of plane. We model this field as

$$\mathbf{F} = \beta V \hat{\nu} + \beta |V| \boldsymbol{\xi}, \quad (4)$$

where β accounts for geometric and dielectric factors that predict a local electric field in the direction $\hat{\nu}$ in response to

an applied voltage V , and $\boldsymbol{\xi}$ is a dimensionless vector giving the relative strength and direction of the rectified field, assumed to scale linearly with $|V|$. Because of the long charging time scale, the rectified field $\beta |V| \boldsymbol{\xi}$ does not change when we switch the bias polarity on millisecond time scales while the dielectric component $\beta V \hat{\nu}$ changes sign, producing a polarity-asymmetric response. The assumption of a linear relationship between the rectified field strength and $|V|$ is motivated by the empirical observation that $\bar{\nu}$, proportional to F_z , varies linearly with applied bias in all our measurements. This amounts to an approximation that the spatial distribution of photoionized charge remains fixed, while the charge density varies linearly with $|V|$.

Figure 2(c) shows the mean ($\bar{\nu}$) and difference (δ) of the transition frequencies extracted from fits to the PLE spectra in Fig. 1(d). The NV-center symmetry axis ($[11\bar{1}]$ in this case) is uniquely determined by the sign of $\bar{\nu}$ in response to electric fields in different directions. By substituting Eq. (4) into Eqs. (3) and applying the appropriate coordinate transformation, we obtain a model that quantitatively agrees with our observations [17], as shown by the fits to the data in Fig. 2(c). Given that this is only a simplified phenomenological description of a complicated three-dimensional system, it matches our observations surprisingly well.

Finally, we present a control experiment in which we mitigate effects due to the 532 nm repump cycle. Occasional repump pulses are still required to compensate for photoionization of the NV^- charge state due to sequential two-photon absorption, but with weak (< 1 nW) resonant light, the required repump period can be increased to several seconds [4], allowing time to apply bias, record a complete PLE spectrum, and rezero the bias, all between repump pulses. Since weak spin-nonconserving optical transitions quickly polarize the NV-center spin away from resonance in the absence of the repump cycle, we mix the spin population by applying a microwave magnetic field resonant with the GS spin transition. We use another device for this purpose (device C), shown in Fig. 2(d), which is fabricated on the same diamond as our four-gate lateral device. It consists of a short-terminated waveguide to generate microwave fields and serve as ground, and a gate that when biased produces lateral electric fields across an 8 μm gap.

Figure 2(d) shows $\bar{\nu}$ and δ as a function of gate voltage for the NV center circled in the inset. Once again the bias polarity is switched at 1 kHz and the PLE photons are binned accordingly. A polarity asymmetry is clearly observed when the repump beam is present, particularly as a kink in $\bar{\nu}$, and it is significantly reduced when the biases are applied in the absence of the repump cycle. Fits to the data using our model [17] are shown as solid curves, from which we find that $|\boldsymbol{\xi}|$ is reduced from 0.71 ± 0.02 with the standard repump cycle to 0.33 ± 0.03 when the 532 nm beam is omitted.

Based on this understanding, we can exploit the photoinduced charge to obtain greatly enhanced tunability in our four-gate geometry (device A). Since the rectified field points predominantly out of plane and has strength comparable to the

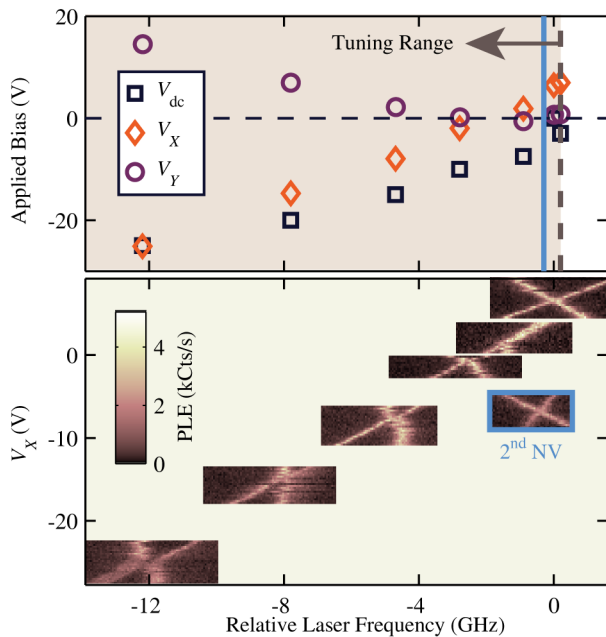


FIG. 3. Tuning diagram for the NV center marked in Fig. 1(c). Degeneracy is achieved at different frequencies by setting the applied biases (V_{dc} , V_X , V_Y) as marked in the upper panel; in the lower panel we show PLE spectra as a function of V_X around each of these points for fixed V_{dc} (V_Y is also varied to keep the ratio V_X/V_Y constant). We can shift a second NV center to degeneracy within the tuning range of the first, as shown by the PLE spectra outlined in blue (lower panel) and the corresponding blue line (upper panel) marking the degenerate frequency.

dielectric component, we effectively obtain three-dimensional control of the local electric field vector. The application of a negative reference bias V_{dc} as shown in Fig. 1(c) increases the rectified component F_Z independently of (F_X, F_Y) . As a demonstration of the flexibility of this technique, we present a tuning diagram in Fig. 3 in which we use (V_X, V_Y) to scan through the C_{3v} degeneracy point at different settings of V_{dc} . Each crossing occurs at a different frequency, with the corresponding bias point (V_X, V_Y, V_{dc}) marked in the upper panel. Essentially, we are compensating the transverse components (S_{E_x}, S_{E_y}) of the intrinsic fields and tuning the longitudinal component of \mathbf{F} to shift the frequency. Since the rectified field always points along $+Z$, we can only tune the frequency in one direction, but the effect is strong enough to produce a >10 GHz shift in the degenerate frequency with practical applied voltages.

With this technique we can tune multiple NV centers to have the same degenerate transition frequency. The PLE spectra outlined in blue in Fig. 3 were obtained from a second NV center in the same device at $V_{dc} = 0$ V and display C_{3v} degeneracy at a frequency within the tuning range of the first. If these two NV centers were in separately controlled devices and tuned simultaneously to degeneracy at the same frequency, they would couple identically to indistinguishable photons.

In conclusion, we have used electric fields to tune the ZPL transitions of individual NV centers in micron-scale devices size compatible with photonic structures. Through their dc Stark shifts, NV centers serve as nanoscale probes of their electrostatic environment, revealing strong signatures of charge accumulation due to photoionization of deep donor levels in the diamond. We have analyzed these effects with a phenomenological model and used the additional fields provided by photoionization to obtain three-dimensional control of the local electric field, in order to tune both the overall energy and orbital splitting of the excited-state Hamiltonian. In particular, we have demonstrated how to reach the C_{3v} symmetry point and then apply longitudinal perturbations to shift the degenerate photon energy. By coupling multiple NV centers to indistinguishable photons with this technique, photonic networks could provide a quantum bus to coherently couple distant NV centers, and entanglement swapping protocols [8] could enable long-distance quantum key distribution.

We acknowledge financial support from the AFOSR, ARO, and DARPA, and thank R. Hanson, C. G. Van de Walle, U. K. Mishra, K. Ohno, and D. J. Christle for useful discussions.

* These authors contributed equally to this work

† Corresponding author.

Email address: awsch@physics.ucsb.edu

- [1] G. Balasubramanian *et al.*, Nat. Mater. **8**, 383 (2009).
- [2] G. D. Fuchs *et al.*, Science **326**, 1520 (2009).
- [3] N. B. Manson, J. P. Harrison, and M. J. Sellars, Phys. Rev. B **74**, 104303 (2006).
- [4] K.-M. C. Fu *et al.*, Phys. Rev. Lett. **103**, 256404 (2009).
- [5] B. B. Buckley, G. D. Fuchs, L. C. Bassett, and D. D. Awschalom, Science **330**, 1212 (2010).
- [6] E. Togan *et al.*, Nature **466**, 730 (2010).
- [7] A. Faraon *et al.*, Nat. Photon. **5**, 301 (2011); C. Santori *et al.*, Nanotechnology **21**, 274008 (2010).
- [8] S. D. Barrett and P. Kok, Phys. Rev. A **71**, 060310 (2005); L. Childress, J. M. Taylor, A. S. Sørensen, and M. D. Lukin, Phys. Rev. A **72**, 052330 (2005).
- [9] J. R. Maze *et al.*, Nature **455**, 644 (2008); G. Balasubramanian *et al.*, Nature **455**, 648 (2008); B. J. Maertz *et al.*, Appl. Phys. Lett. **96**, 092504 (2010).
- [10] F. Dolde *et al.*, Nat. Phys. **7**, 459 (2011).
- [11] A. Batalov *et al.*, Phys. Rev. Lett. **102**, 195506 (2009).
- [12] E. Van Oort and M. Glasbeek, Chem. Phys. Lett. **168**, 529 (1990).
- [13] P. Tamarat *et al.*, Phys. Rev. Lett. **97**, 083002 (2006); New J. Phys. **10**, 045004 (2008).
- [14] M. W. Doherty, N. B. Manson, P. Delaney, and L. C. L. Hollenberg, New J. Phys. **13**, 025019 (2011); J. R. Maze *et al.*, New J. Phys. **13**, 025025 (2011).
- [15] The NV-center coordinate system is chosen such that \hat{z} points along the N-V symmetry axis and \hat{x} lies in a reflection plane.
- [16] Note that while spin-spin coupling leads to mixed ES spin eigenstates in some regimes, it does not significantly affect the optical pumping mechanism which polarizes the spin into $|S_z\rangle$ in our experiments.
- [17] See supporting online material.

- [18] J. Isberg, A. Tajani, and D. J. Twitchen, Phys. Rev. B **73**, 245207 (2006).
- [19] R. G. Farrer, Solid State Commun. **7**, 685 (1969); J. Rosa, M. Vaněček, M. Nesládek, and L. M. Stals, Diam. Relat. Mater. **8**, 721 (1999).
- [20] F. J. Heremans *et al.*, Appl. Phys. Lett. **94**, 152102 (2009).

Supplemental Material for “Electrical Tuning of Single Nitrogen-Vacancy Center Optical Transitions Enhanced by Photoinduced Fields”

L. C. Bassett, F. J. Heremans, C. G. Yale, B. B. Buckley, and D. D. Awschalom
Center for Spintronics and Quantum Computation,
University of California, Santa Barbara, CA 93106, USA
(Dated: May 29, 2018)

METHODS AND SUPPLEMENTARY DATA

Optical methods

Measurements were performed using two home-built confocal microscopes designed to excite single NV centers both resonantly at 637.2 nm and in the blue-shifted phonon sideband at 532 nm, while collecting photoluminescence photons from the red-shifted photoluminescence sideband between $\approx 650\text{--}830$ nm. Details and a schematic are available elsewhere [1]. The 532 nm laser serves both as the excitation for standard photoluminescence spatial imaging and as a ‘re-pump’ cycle to maintain the NV^- charge state which is photoionized by resonant excitation alone.

Resonant excitation is provided by tunable diode lasers from the New Focus VelocityTM series, which are tuned by means of a piezoelectric actuator that makes fine adjustments to the laser cavity. An important technical aspect of these experiments is the calibration of the laser frequency response to variations in the voltage applied to the piezo, since this is typically nonlinear and hysteretic. In one of our microscope setups we have pre-calibrated the laser frequency response to particular piezo modulation sequences using a Mach-Zehnder interferometer. In the other setup, unpredictable mode hops of the laser make such calibrations unreliable, so we continuously monitor the laser frequency interferometrically: a Fabry-Perot cavity with a free spectral range of 1.5 GHz provides fine frequency resolution, while a Mach-Zehnder interferometer with free spectral range ≈ 7 GHz is used to detect mode hops. In both cases, our calibrations provide relative frequency determinations with ≈ 100 MHz uncertainty across the ≈ 90 GHz piezo modulation range. The resonant light is prepared with circular polarization, so that the (linear) optical selection rules for $|S_z\rangle$ optical transitions do not cause the resonances to disappear in certain regimes.

In both setups, we also have the ability to add confocal excitation at 405 nm (3.1 eV) to the optical path. Unsurprisingly, this higher-energy excitation significantly alters the charging dynamics of the system. Generally it causes the NV center optical transitions to become less stable and so it was not used during any of the measurements presented in the main text, but we did use it as a control to ‘reset’ the equilibrium charge distribution with no applied bias between experiments. A short burst of 405 nm light applied in this configuration was generally enough to restore the initial NV center transition frequen-

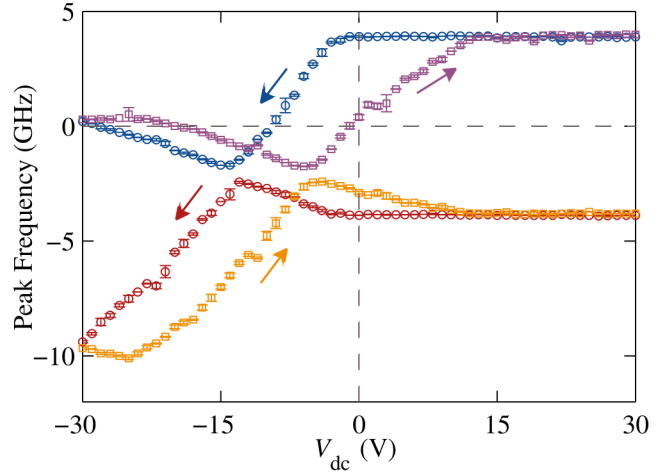


FIG. S1. Stark shift hysteresis loop for the NV center marked in Fig. 1c of the main text as a function of V_{dc} (with $V_X, V_Y = 0$). Points mark the optical resonance frequencies extracted from two-Lorentzian fits to PLE spectra at the corresponding voltage, and color-coded arrows mark the sweep direction. Errorbars represent the frequency uncertainties from the fits.

cies (≈ 10 s at optical power ≈ 10 μW), while full relaxation in the presence of the 532 nm light alone required several hours.

Charging behavior in device A

The interpretation of the hysteresis measurements presented in the main text (Fig. 2a) is simplified by the one-dimensional geometry of the top-gate device, but we measured a qualitatively similar response in our four-gate lateral device (device A, see Fig. 1c in the main text) to variations of the reference voltage V_{dc} common to all four gates. Figure S1 shows a hysteresis loop as a function of V_{dc} for the NV center marked in Fig. 1c, which is ≈ 7 μm below the diamond surface. Although the response is similar to the top-gate measurements we do notice a few differences: First, the hysteresis ‘direction’ is reversed, in the sense that the Stark response lags V_{dc} in Fig. S1, while it leads the top-gate bias in Fig. 2a. Second, the ‘threshold bias’ is closer to zero in the lateral device than in our top-gate measurements. These differences are probably due to a variety of factors, including (a) geometric differences due to the gate geometry and the depths of the

respective NV centers, (b) variations in the diamond samples, (c) details of the diamond-metal interfaces for different metals (Ti/Pt/Au on the lateral device and indium-tin-oxide as the top gate), and perhaps most importantly (d) the electrostatic boundary conditions at the back of the device – the top-gate device *B* is indium-bonded to ground on the backside, while device *A* is glued to the ground plane with an insulating adhesive.

We note that polarity-dependent Stark shifts have been recently observed for Chromium centers in diamond [2], and suggest that a one-dimensional experiment with a transparent top gate could determine whether these devices display similar charging behavior.

Photoconductivity

When voltages are applied between surface gates in the presence of optical excitation, we expect the photoexcitation of defect levels to lead to a photocurrent near the surface. Fig. S2 shows the photoconductivity response of device *A* when the excitation beam is focused on the NV center marked in Fig. 1c of the main text, 6 μm below the diamond surface. The top panel shows an example of a typical dc photoconductivity response for this and similar devices we have measured, with almost no measurable current flowing in the dark and typical photocurrents of a few nanoamperes when the excitation beam is applied. On this particular device, a larger current ‘leak’ existed between the left and lower gates, as shown in the lower panel of Fig. S2. When $V_{\text{Lower}} - V_{\text{Left}} \gtrsim 20$ V, a current of several microamperes flows between them.

It is important to note, however, that the presence of a photocurrent between gates near the diamond surface does not preclude the accumulation of a space charge deeper in the sample, especially since photoexcited charge transport through diamond is an inefficient process, and the timescales for charge storage are very long [3]. As illustrated schematically in Fig. 2b of the main text, the out-of-plane component of the photoinduced field is primarily due to positive charge from photoionized donors *below* the NV center, which results from the effective voltage applied *across the sample* rather than between two lateral gates. Thus even with a substantial leak between two gates, both the dielectric and photoinduced components of the dc Stark shift are always present. Practically, however, photocurrents may lead to local heating of the sample, and we attribute the leak between the left and lower gates to the broadening of the PLE resonances observed in Fig. 3 of the main text when larger lateral voltages are applied.

ANALYSIS OF DC STARK SHIFTS

The first step in the analysis of dc Stark shifts in our devices is a determination of the NV center’s orientation in the diamond crystal. This may be any of the eight projections

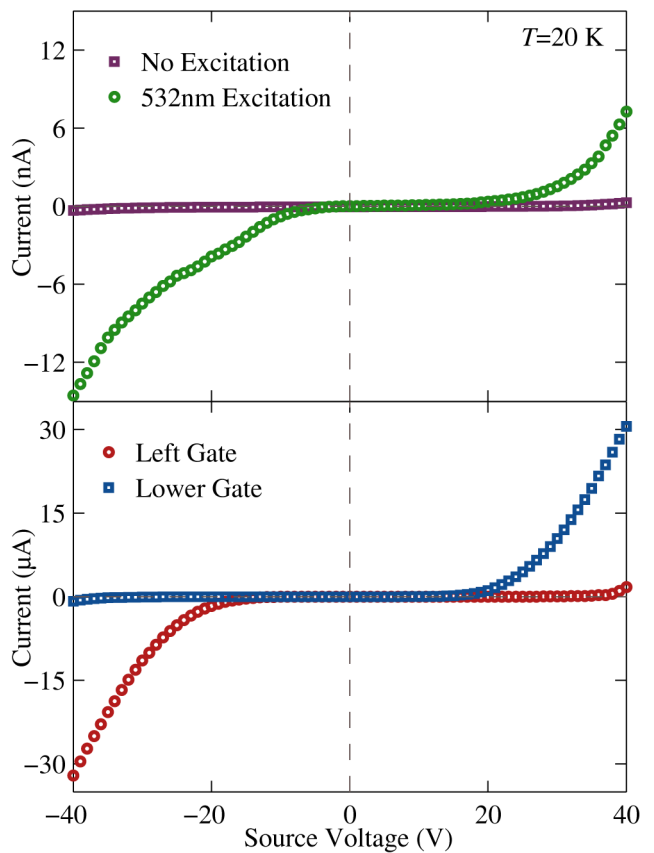


FIG. S2. Top panel: I - V curves showing conductivity between gate the right-hand gate of device *A* (see Fig. 1c in the main text) and the remaining three surface gates, both with (green circles) and without (purple squares) 532 nm excitation. Lower panel: Similar photoconductivity measurements (excitation applied) with the bias connected to the left-hand gate (red circles) and lower gate (blue squares), showing a larger leakage current between these two gates.

from the $\langle 111 \rangle$ family; note that antiparallel (i.e., N-V compared to V-N) orientations are distinguishable due to the permanent dipole in the z direction. Using the coordinate systems described in the text, we note that N-V axis projects either in the $\pm X$ or $\pm Y$ sample directions, and also has a component along $\pm Z$. We can therefore label a given orientation by (p_X, p_Y, p_Z) , where $p_{X,Y} = 0, \pm 1$ give the sign of the N-V projection in the (X, Y) axes (note $p_X^2 + p_Y^2 = 1$) and $p_Z = \pm 1$ gives the sign of the Z -projection. For a given NV center, we can determine whether p_X or p_Y equals zero from the dependence of the photoluminescence on the linear polarization of the 532 nm repump beam (the photoluminescence is a maximized when the light is polarized perpendicular to the N-V axis). It is then usually straightforward to determine the exact projection from the slope of the longitudinal dc Stark component $\bar{\nu}$ in response to applied voltages, keeping in mind that the rectified field points mainly out of plane. For example, we know from polarization measurements that the NV center of Fig. 1 projects in the $\pm X$ direction, and from the sign of $\bar{\nu}$ in response to V_X (Fig. 2c) we see that $p_X = +1$

and $p_Z = -1$, corresponding to the crystal direction $[11\bar{1}]$ as depicted in the schematic of Fig. 2b.

Given the NV-center symmetry axis, the transformation be-

tween sample and NV-center coordinate systems is given by

$$\mathbf{F}_{\text{NV}} = \mathbf{M}\mathbf{F}_{\text{Sample}}, \quad (\text{S1})$$

where \mathbf{M} is the rotation matrix

$$\mathbf{M} = \frac{1}{\sqrt{3}} \begin{pmatrix} p_X & p_Y & -\sqrt{2}p_Z \\ -\sqrt{3}p_Y p_Z & \sqrt{3}p_X p_Z & 0 \\ \sqrt{2}p_X & \sqrt{2}p_Y & p_Z \end{pmatrix}. \quad (\text{S2})$$

Applying this transformation for the NV center in our lateral device, we obtain expressions for the dc Stark components $\bar{\nu}$ and δ in terms of the local field in sample coordinates:

$$h\bar{\nu} = \hbar\omega_0 + \frac{\Delta\mu_{\parallel}}{\sqrt{3}} \left(\sqrt{2}F_X - F_Z \right), \quad (\text{S3a})$$

$$h\delta = \sqrt{2} \left\{ \left[S_{E_x} - \frac{\mu_{\perp}}{\sqrt{3}} \left(F_X + \sqrt{2}F_Z \right) \right]^2 + \left[S_{E_y} - \mu_{\perp} F_Y \right]^2 \right\}^{1/2}. \quad (\text{S3b})$$

By expressing the local field according to our model as $\mathbf{F} = \beta V \hat{\mathbf{v}} + \beta |V| \boldsymbol{\xi}$, we obtain a dependence on applied bias that we can quantitatively compare to our measurements.

To reduce the number of free parameters, we fix the components of the dielectric unit vector $\hat{\mathbf{v}}$ based on electrostatic simulations of our device using the COMSOL MULTIPHYSICS[®] software. For a single set of measurements (e.g., $\bar{\nu}$ and δ as a function of bias along a single direction), this leaves eight free parameters: $\{\omega_0, S_{E_x}, S_{E_y}, \beta\Delta\mu_{\parallel}, \mu_{\perp}/\Delta\mu_{\parallel}, \xi_X, \xi_Y, \xi_Z\}$. This equals the combined number of free parameters expected for the form of both $\bar{\nu}$ and δ (i.e., two lines and two hyperbolae constrained to meet at $V = 0$) and so results in a well-conditioned minimization problem. When we have multiple measurements of the same NV center, e.g., for the repump/no repump measurements in Fig. 2d, we can constrain the parameters even further, and require that $\{\omega_0, S_{E_x}, S_{E_y}, \beta\Delta\mu_{\parallel}, \mu_{\perp}/\Delta\mu_{\parallel}\}$ are common for each NV center, while only the rectification vector $\boldsymbol{\xi}$ varies independently for each set. In the case of the lateral measurements of Fig. 2c, we also allow the dielectric coefficient β to vary between the V_X and V_Y measurements, and the resulting best-fit parameters for a combined fit as described above are listed in Table I. As expected, the rectified field points mainly in the $+Z$ direction.

Electrostatics of the photoinduced fields

A full description of the photoinduced fields in our devices is beyond the scope of this work, especially since our phenomenological model seems to capture the behavior important for controlling NV-center Stark shifts in these geometries. Such a description would presumably need to account for the gate geometries of our devices, the variation of optical intensity through the sample in a confocal geometry, trans-

port dynamics of photoexcited charges, and potentially spatial inhomogeneities in the distribution of deep donors. Furthermore, although we expect that substitutional nitrogen atoms dominate the electrostatics, other defect centers may also play an important role, such as vacancy complexes unintentionally created during the irradiation and annealing process. Based on the electron irradiation dose used, we expect a vacancy concentration (before annealing) of $\approx 6 \times 10^{13} \text{ cm}^{-3}$ [4], which is roughly an order of magnitude less than the nitrogen concentration in these samples, and these acceptor defects probably have an effect on the transport of photoionized charge through the sample. Still, we can gather some quantitative information about the photoinduced charge distributions from the NV-center Stark response, which we can compare to a simplified ‘band-bending’ model treating the device as a Schottky diode.

The top-gate geometry of device *B* is the simplest to analyze, and as mentioned in the text we can compare the magnitudes of the dc Stark shifts observed in that device (Fig. 2a) with those of device *A* (Fig. 2c) to estimate the local electric field strength. Assuming that in the top-gate device the local electric field points only in the $+Z$ direction, we relate the slope of $\bar{\nu}$ to the local electric field $F_Z = \beta_Z V$ through the relation

$$\frac{d\bar{\nu}}{dV} = \frac{\beta_Z \Delta\mu_{\parallel}}{\sqrt{3}h}, \quad (\text{S4})$$

where the factor $1/\sqrt{3}$ appears due to the projection of the NV-center symmetry axis in the sample. Below the threshold bias in Fig. 2a, $d\bar{\nu}/dV \approx 0.06 \text{ GHz/V}$. In comparison, from the fits to the lateral data in Fig. 2c described in the previous section, we find that the dielectric response of device *A* is $\beta_{\text{Lateral}} \Delta\mu_{\parallel}/h \approx 0.2 \text{ GHz/V}$. Therefore the ratio of the dielectric field in device *A* to the rectified field in device *B* is $\beta_{\text{Lateral}}/\beta_Z \approx 2$, while from dielectric response alone this ra-

TABLE I. Best-fit parameter values from fits of our model to the data in Fig. 2c in the main text, for Stark shifts as a function of applied bias (V_X, V_Y) in orthogonal directions. Uncertainties are at 95% confidence from the fit alone, and do not include systematic errors due to the somewhat strong covariance between many of these parameters and the uncertainty in the fixed direction \hat{v} of the dielectric field. Based on electrostatic modeling, we use $\hat{v} = (0.998, 0.04, 0.07)$ and $(-0.002, 0.9998, 0.02)$ for the V_X and V_Y dependence, respectively.

	Common parameters	Direction-dependent parameters	Bias direction	
			V_X	V_Y
$\omega_0/2\pi$	0.66 ± 0.03 GHz	$\beta\Delta\mu_{\parallel}/h$	0.334 ± 0.002 GHz/V	0.175 ± 0.003 GHz/V
S_{E_x}/h	5.06 ± 0.03 GHz	ξ_X	0.15 ± 0.01	0.19 ± 0.02
S_{E_y}/h	0.78 ± 0.06 GHz	ξ_Y	-0.43 ± 0.02	-0.30 ± 0.02
$\mu_{\perp}/\Delta\mu_{\parallel}$	1.41 ± 0.02	ξ_Z	1.01 ± 0.01	1.60 ± 0.02

tio should be ≈ 100 , corresponding to an enhancement of the vertical electric field below the top gate by a factor of ≈ 50 .

If we picture the top-gate device as a Schottky diode, this comparison suggests that when negative (reverse) bias is applied, the potential drops across a distance of only ≈ 10 μm rather than the full 0.5 mm thickness of the sample. Assuming uniform ionization of deep donors with density N_d , the equivalent Schottky ‘depletion width’ obtained from the solution to Poisson’s equation is given by [5]

$$w_d = \sqrt{\frac{2\epsilon\epsilon_0|\varphi|}{eN_d}}, \quad (\text{S5})$$

in terms of the Schottky barrier height φ and diamond’s dielectric constant $\epsilon \approx 5.7$. For $w_d \approx 10$ μm and $\varphi \approx 10$ V, this estimate yields an ionized charge density of $N_d \approx 6 \times 10^{13} \text{ cm}^{-3}$, which is in agreement with a $\approx 10\%$ ionization of the anticipated substitutional nitrogen concentration of a few parts per billion ($\approx 1 \times 10^{15} \text{ cm}^{-3}$). This rough calculation shows that the photoinduced fields we observe are consistent with the expected concentration of deep defects, although it does not account for nonlinearities in the distribution of photoionized charge. For example, we observe a qualitatively similar enhancement of the Z -direction field when focussed on NV centers up to ≈ 50 μm below the top gate, suggesting that the charge distribution is not confined to a layer near the surface gate but rather follows the region of higher optical intensity.

The role of the repump cycle on photoinduced fields

As described in the main text, we performed a control experiment to investigate the influence of the 532 nm repump cycle on the rectified component of the local electric field. Using the device shown in Fig. 2d, we apply a microwave current through a short-terminated waveguide resonant with the ground-state $|S_z\rangle \leftrightarrow \{|S_x\rangle, |S_y\rangle\}$ transition at 2.878 GHz. This maintains a mixed spin state during our measurements since, in the absence of the repump cycle, weak spin-nonconserving transitions would otherwise polarize the spin away from resonance with the red laser. In the PLE spectra (Fig. S3), we therefore observe the spin-conserving optical transitions for all three triplet spin states. We isolate the $|S_z\rangle$

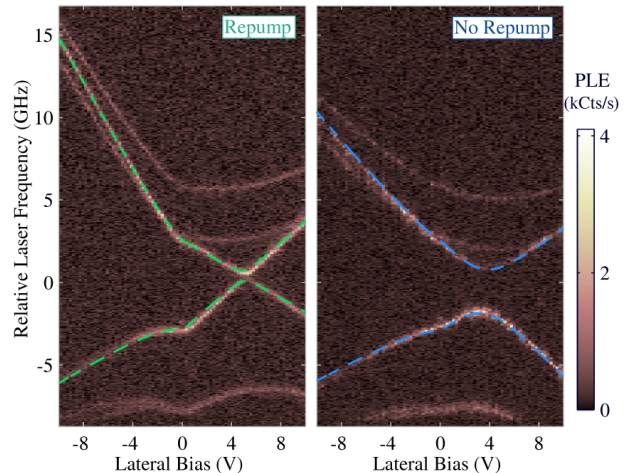


FIG. S3. PLE spectra as a function of gate voltage, for the NV center circled in Fig. 2d, both with the standard 532 nm repump cycle (left) and with only intermittent repump pulses applied at zero bias (right). The $|S_z\rangle$ transition frequencies reconstructed from the fits shown in Fig. 2d are overlaid (dashed curves). Other resonances visible in these spectra correspond to spin-conserving optical transitions for the $\{|S_x\rangle, |S_y\rangle\}$ spin states, as described in the text.

resonance frequencies from fits to these PLE spectra to compute the dc Stark components $\bar{\nu}$ and δ plotted in Fig. 2d of the main text. These are marked by dashed curves in Fig. S3, which are the resonance frequencies reconstructed from the best-fit results of our model plotted in Fig. 2d. The analysis leading to the fits is similar to that described above (in this case the NV-center projection is $[1\bar{1}1]$), and the best-fit parameters are listed in Table II.

- [1] B. B. Buckley, G. D. Fuchs, L. C. Bassett, and D. D. Awschalom, *Science* **330**, 1212 (2010).
- [2] T. Müller, I. Aharonovich, L. Lombez, Y. Alaverdyan, A. N. Vamivakas, S. Castelletto, F. Jelezko, J. Wrachtrup, S. Prawer, and M. Atatüre, *New J. Phys.* **13**, 075001 (2011).
- [3] C. E. Nebel, M. Stutzmann, F. Lacher, P. Koidl, and R. Zachai, *Diam. Relat. Mater.* **7**, 556 (1998); F. J. Heremans, G. D. Fuchs, C. F. Wang, R. Hanson, and D. D. Awschalom, *Appl. Phys. Lett.* **94**, 152102 (2009).

TABLE II. Best-fit parameter values from fits of our model to the data in Fig. 2d in the main text, investigating the role of the 532 nm repump laser on the photoinduced field. As in Table I, uncertainties are quoted at 95% confidence from the fit, but do not account for covariance between the fit parameters and the direction of the dielectric field, fixed to $\hat{v} = (0.97, 0.04, -0.24)$ based on electrostatic modeling.

	Common parameters	Repump-dependent parameters	With repump	Without repump
$\omega_0/2\pi$	-0.17 ± 0.02 GHz	ξ_x	-0.239 ± 0.009	0.06 ± 0.01
S_{E_x}/h	-2.34 ± 0.09 GHz	ξ_y	0.12 ± 0.01	0.13 ± 0.02
S_{E_y}/h	3.08 ± 0.05 GHz	ξ_z	0.66 ± 0.02	0.30 ± 0.03
$\mu_{\perp}/\Delta\mu_{\parallel}$	0.91 ± 0.01			
$\beta\Delta\mu_{\parallel}/h$	0.99 ± 0.01 GHz/V			

[4] D. J. Twitchen, D. C. Hunt, V. Smart, M. E. Newton, and J. M. Baker, *Diam. Relat. Mater.* **8**, 1572 (1999).

[5] C. Kittel, *Introduction to Solid State Physics*, 7th ed. (John Wiley & Sons, Inc., 1996) p. 574.